PCCP

Accepted Manuscript

ROYAL SOCIETY OF CHEMISTRY

www.rsc.org/pccp

Structure and stability of reduced and oxidized mononuclear platinum species on nanostructured ceria from density functional modeling

Hristiyan A. Aleksandrov,[1,2] Konstantin M. Neyman,[2,3] and Georgi N. Vayssilov[1*]

[1] Faculty of Chemistry and Pharmacy, University of Sofia, 1126 Sofia, Bulgaria
e-mail: gnv@chem.uni-sofia.bg

[2] Departament de Química Física & Institut de Química Teòrica i Computacional (IQTC-UB), Universitat de Barcelona, 08028 Barcelona, Spain

[3] Institució Catalana de Recerca i Estudis Avançats (ICREA), 08010 Barcelona, Spain
e-mail: konstantin.neyman@icrea.cat

Abstract

We report our results for the structure and relative stability of mononuclear platinum species on a ceria nanoparticle $Ce_{21}O_{42}$ depending on reduction or oxidation of the system. The most stable platinum species is Pt^{2+} at small {100} facets, where the ion is coordinated in a square-planar complex with four oxygen anions as ligands. Partial reduction of the system does not affect the state of platinum in this position but causes reduction of cerium ions. Atomic platinum species in all other modeled positions on the surface of the ceria nanoparticle are found to be in the oxidation state 0. Based on the calculated thermodynamic quantities we analyzed the formation of preferable type of platinum species depending on the temperature and O_2 pressure. Our thermodynamic model show that the most stable species at standard conditions is PtO, while at the partial pressure of O_2 below 100 Pa the stoichiometric complex $Pt/Ce_{21}O_{42}$ is formed. In both structures there is Pt^{2+} located in a square-planar complex. The characteristics of these two structures fit well to the available EXAFS and XPS data. These structures are energetically stable with respect to sintering, while the agglomeration to platinum clusters is exothermic for the neutral mononuclear Pt species located at {111} facets.

1 Introduction

Ceria is a component of various important catalysts for conversion of harmful automotive exhaust gases into non-toxic ones,[1,2] water gas shift reaction (WGSR),[3,4] preferential CO oxidation,[5,6] reforming of alcohols,[7] fuel cell processes,[8] etc. The catalytic role of ceria is mainly related with its reducibility, i.e. when it is heated to sufficiently elevated temperatures O vacancies (O_{vac}) are created and for each O vacancy two Ce^{4+} ions are reduced to Ce^{3+}. The process is reversible, depending on the conditions (partial pressure of O_2 or another oxygen supplier and temperature).

Another important component of ceria based catalysts is a transition (noble) metal deposited on the ceria support. One of the commonly used metals is Pt. Hence, it is not surprising that numerous experimental studies are devoted to clarify the structures and properties of Pt/CeO_2 systems. For instance, Hatanaka et al.[9] showed that Pt on ceria can change reversibly its oxidation state depending on the conditions: the oxidation state is +2 or +4 at oxidation conditions and zero at reductive conditions. Recently, Bruix et al.8 have predicted theoretically and identified experimentally that mononuclear Pt^{2+} species can exist on ceria nanoparticles. Moreover those ionic species may be crucial for the catalytic activity of Pt/CeO_2 systems.3,8,[10]

Calculations of Pt/CeO_2 systems predicted a charge transfer from platinum clusters to the ceria support, which leads to formation of Ce^{3+} ions. [11-14] It was also shown that O spillover from ceria to the adsorbed Pt clusters is a favorable process when nanoparticle ceria is used and is not favorable when Pt clusters are deposited on large ceria particles, which were approximated with periodic slab models.[13] Very recently, globally optimized structures of Pt_6 clusters deposited on a regular $CeO_2(111)$ surface were shown to bind atomic O transferred from the support essentially without any energy lost.[11] Interactions of O, CO, and H species with $Pt_{10}/CeO_2(111)$ and mechanisms of WGSR were also modeled computationally.[15,16] Less attention is devoted to mononuclear Pt species deposited on ceria.[17] As mentioned above8 it was found that Pt^{2+} ionic species can be formed, which show that charge transfer from Pt to ceria is possible not only for Pt clusters, but also for mononuclear species. Ionic Pt is also modeled at doping CeO_2, where Pt occupies surface or bulk position of Ce^{4+} ion.[18]

In the present theoretical study, we modeled mononuclear Pt species on $Ce_{21}O_{42}$ nanoparticle. Our goal was to understand, which is the most stable position of the mononuclear Pt species interacting with stoichiometric, reduced and oxidized ceria

nanoparticles. Based on the calculated relative energies we analyzed the resistance/preference of the mononuclear platinum species with respect to sintering and determined, which of them are the most stable depending on the experimental conditions, $p(O_2)$ and T. The structural features and estimated Pt 4f core level energies of different modeled systems are compared with available experimental data.

2 Computational method and models

The calculations are performed with periodic plane-wave density functional method using a GGA exchange-correlation functional PW91,[19] as implemented in VASP code.[20-22] An on-site Coulombic correction ($U_{eff} = U-J$)[23,24] is applied within the GGA+U scheme to all Ce atoms to obtain a localized description of Ce 4f-electrons in reduced Ce^{3+} ions. In line with previous studies[8,12-14,25] the U_{eff} value of 4.0 eV is used. A plane-wave basis with a 415 eV cut-off for the kinetic energy and projector-augmented wave[22] description of core-valence electron interactions are employed. Our model ceria nanoparticle $Ce_{21}O_{42}$ has a diameter of about 1 nm.[26,27] A cubic 2.0 × 2.0 × 2.0 nm unit cell is employed. Thus, each nanoparticle is separated from its periodically repeated images in the neighboring unit cells in the three Cartesian directions by at least 0.9 nm to minimize interactions between the nanoparticles. Γ-point calculations are performed. Single-point total energy convergence tolerance at the self-consistency is set to 10^{-6} eV and structure optimizations continued until the maximum forces acting on each atom were less than 0.02 eV/Å. Where appropriate, spin-polarized calculations were performed in order to account for the reducibility of the Ce^{4+} ions.

A Pt atom was considered in different surface positions of the ceria nanoparticle. In the modeled systems we also included one or two additional oxygen atoms (O_{add}) near the platinum in order to generate oxidized mononuclear platinum species, Pt^{2+} or Pt^{4+}, respectively. The latter structures mimic deposition of neutral PtO or PtO_2 species on ceria. The formal charge of the platinum species and the number of Ce^{4+} cations reduced to Ce^{3+} are determined by the condition of the electro-neutrality of the whole system, which for our models can be expressed in terms of atomic concentrations in the nanoparticle (numbers of species) as

$$[Ce^{3+}] + 2\times[O_{add}] - 2\times[O_{vac}] - 2\times[Pt^{2+}] - 4\times[Pt^{4+}] = 0. \qquad (1)$$

Here, respectively, $[O_{vac}]$ and $[O_{add}]$ are the concentrations of the oxygen vacancies and added oxygen atoms, $[Pt^{2+}]$ and $[Pt^{4+}]$ are the concentrations of Pt^{2+} and Pt^{4+} ions, and $[Ce^{3+}]$ is the

concentration of Ce^{3+} ions. Note that the balance in eq. (1) is based on the assumption that the added O atoms become O^{2-} ions in the system, while the equation should be modified if peroxo (O_2^{2-}) or superoxo (O_2^{-}) species[28] are formed. The equation is based on a simple balance of the number of electrons in the system. All structures are denoted according to their sequence in Fig. 1 and the number of O vacancies or additional O centers. For example, the labels c-1v and c-2v denote structures with one and two O_{vac} in ceria nanoparticle and location of Pt species as shown in Fig. 1c, while notations d-1O and d-2O correspond to the structures with location of Pt species as in Fig. 1d and one and two O_{add} centers in the model forming PtO and PtO_2 moiety, respectively.

The vibrational frequencies of the deposited PtO_X species are calculated numerically. No imaginary frequencies are found in all systems.

The reported hereafter binding energies (BE) of the PtO_X (X = 0 – 2) adsorbates to the ceria nanoparticle substrates are calculated as $BE(PtO_X) = - E_{ad} - E_{sub} + E_{ad/sub}$, where E_{ad} is the total energy of the PtO_X (X = 0 – 2) adsorbate in the gas phase, E_{sub} is the total energy of the corresponding bare ceria nanoparticle $Ce_{21}O_{42-Y}$ (stoichiometric, Y = 0, or reduced, Y = 1 – 2), and $E_{ad/sub}$ is the total energy of the $Ce_{21}O_{42-Y}$ substrate interacting with the PtO_X adsorbate. With the above definition, negative values of BE imply exothermic interaction. For comparison of the relative stability of different model systems $PtO_X/Ce_{21}O_{42-Y}$ we also calculated their relative energy, E_{rel}, with respect to the bare stoichiometric ceria nanoparticle, Pt atom and corresponding amount of O_2 molecules in the gas phase:

$$E_{rel} = E[PtO_X/Ce_{21}O_{42-Y}] - (X-Y)/2*E(O_2) - E(Pt) - E(Ce_{21}O_{42}), \quad X = 0 – 2, Y = 0 – 2.$$

We should mention that gradient-corrected DFT functionals do not reproduce well the binding energy of O_2 molecule with respect to two oxygen atoms, typically overestimating it.[29] This may result in reduction of the oxygen vacancy formation energy by about half of eV when it is determined with respect to the half of the calculated energy of O_2 molecule.[30]

From the calculated energy values and pertinent vibrational frequencies we determined thermodynamic quantities for different models and analyzed the preference for their formation depending on the location of the Pt atoms on the ceria nanoparticle, temperature and oxygen pressure in the system. We define the relative Gibbs free energy of a $PtO_X/Ce_{21}O_{42-Y}$ system, $\Delta G(PtO_X/Ce_{21}O_{42-Y})$, via its (formal) formation from the corresponding pristine Pt species, supported on ceria nanoparticle with two O vacancies, $Pt/Ce_{21}O_{40}$, after adsorption of the corresponding number of O_2 molecules from the gas phase:

$$\Delta G(PtO_X/Ce_{21}O_{42-Y}) = \Delta H(PtO_X/Ce_{21}O_{42-Y}) - T\Delta S(PtO_X/Ce_{21}O_{42-Y}).$$

The enthalpy values, $\Delta H(PtO_X/Ce_{21}O_{42-Y})$, were obtained from the total energy values $E_{el}(PtO_X/Ce_{21}O_{42-Y})$ corrected for the internal vibrational energy E_v[31] and zero-point vibrational energy (ZPE) derived from vibrational frequencies of the O_{add} centers and the O centers, which have been subsequently removed to form reduced structures:

$$H = E_{el} + E_v + ZPE.$$

In the calculation of the entropy values of the $PtO_X/Ce_{21}O_{42-Y}$ structures only the electronic (S_{el}) and vibrational (S_v) degrees of freedom were taken into account, since the O adsorbates are bound to the surface sufficiently strongly and the rotational and translational degrees of freedom are converted into vibrations.[32,33] Only for the O_2 molecule in the gas phase translational and rotational contributions E_{tr} and E_{rot} are added to the internal energy and entropy:

$$H(O_2) = E_{el} + E_v + E_{tr} + E_{rot} + ZPE,$$

$$S(O_2) = S_{el} + S_v + S_{tr} + S_{rot}.$$

The expressions for all enthalpy and entropy contributions can be found elsewhere.[31]

3 Results

3.1 Relative stability of stoichiometric, reduced and oxidized species

We modeled four different initial positions of a single Pt atom on the {111} facets and on edges of $Ce_{21}O_{42}$ nanoparticle (Fig. 1). In the first position (a) the Pt atom is on top of a surface O ion. In three other initial structures we put Pt above a triangle of Ce^{4+} ions, where O is in the subsurface position and the Pt atom is in the vicinity of an edge (b) or a corner (c), (d) of the ceria particle. In most of the modeled positions the binding energy (BE) of the metal atom is in the range -2.4 ÷ -3.0 eV (Table 1, a-reg, b-reg, c-reg and d-reg). This is by ~0.5 eV higher in magnitude than the BE of Pt atom calculated in a somewhat different way on CeO_2(111) surface, -1.84 ÷ -2.65 eV.[17] In these three positions Pt atom remains in the oxidation state zero. Note that typically only very limited (if any) charge transfer between single transition metal atoms and regular surfaces of non-reducible metal-oxide supports takes place.[34]

In addition to the {111} facets and the edges our model ceria nanoparticle exposes a specific surface site at the crossing of four {111} facets. It forms squares of four Ce^{4+} ions and of four O^{2-} ions, i.e. a very small {100} facet. When Pt atom is in the center of this square of four oxygen ions, (see Fig. 1e), positions of these ions are adjusted during the geometry optimization to accommodate the atomic Pt in a square-planar complex. Since square-planar complexes are typical for ionic Pt^{2+} species, the most stable electronic state of platinum in position (e) is not Pt^0 but Pt^{2+}, as it was recently reported.[8] The Pt^{2+} cation is formed via transfer of two electrons from platinum to ceria nanoparticle resulting in reduction of two ions Ce^{4+} to Ce^{3+}. This position with BE(Pt) = -5.5 eV (see data for e-reg species in Table 1) is the most stable for the modeled monoatomic platinum, over 2.0 eV more stable than the Pt^0 species in the other studied positions (e.g. compared with a-reg species in Table 1).

We modeled a reduced state of the $Pt/Ce_{21}O_{42}$ system by the ceria nanoparticle with one or two oxygen vacancies. The oxygen atoms were removed from the positions where they were found to be the least bound in the bare $Ce_{21}O_{42}$ nanoparticle, i.e. low-coordinated O atoms.[26,27] In the structures (a)-(d) we removed one or two O centers from the small {100} facet, while in the structure (e), we removed O centers from the opposite side of the particle, since Pt^{2+} interacts with the four O atoms of the {100} facet. From these calculations we estimated the BE of Pt to the reduced nanoparticle in the corresponding positions, and also the energy required for the oxygen vacancy formation in the presence of the platinum species.

There is no clear trend for the influence of the O vacancies on the BE of platinum in positions (a)-(d) (see the variations of the $BE(PtO_X)$ values in Table 1). In the most stable position of Pt, (e), the BE(Pt) value for e-1v and e-2v is lower than that on the bare $Ce_{21}O_{42}$ nanoparticle, e-reg, by 0.25 and 0.39 eV for the first and second vacancy, respectively. Thus, Pt binds weaker to the reduced particle than the stoichiometric one. This suggests that the presence of monoatomic Pt species makes the reduction of ceria nanoparticle somewhat more difficult compared to pristine particle. This effect is similar to what has been reported for Pt_8 cluster deposited on the $Ce_{40}O_{80}$ nanoparticle[13] or on $CeO_2(111)$ surface.[12] However, Pt_8 cluster on the same ceria nanoparticle as in the present study, $Ce_{21}O_{42}$, induced decrease of energy required for oxygen vacancy formation from 1.67 to 1.23 eV, i.e. by 0.44 eV.[14] For Pt atoms and clusters interacting with the reduced ceria nanoparticle the BE of Pt atoms decreases with respect to stoichiometric one, while the BE of Pt_8 cluster increases. This indicates that reduced state of the ceria nanoparticle thermodynamically promotes deposition of platinum clusters, but disfavors deposition of atomic Pt.

The most stable location of Pt in the reduced ceria nanoparticle remains {100} facet (Fig. 1e) despite the weakened binding. In the reduced structures with one and two oxygen vacancies platinum does not change its 2+ state and the whole system contains 4 or 6 Ce^{3+} cations for one or two vacancies, respectively.

On the reduced models with one (1v) and two (2v) oxygen vacancies we also considered insertion of Pt atom in the O_{vac} space (see Fig. 1f). In the complex f-1v with one O vacancy, $Pt/Ce_{21}O_{41}$(f), Pt^{2+} is in a square planar coordination. Interestingly, according to its E_{rel} value -1.47 eV, the structure $Pt/Ce_{21}O_{41}$(f) was calculated to be at least 0.4 eV more stable than the corresponding reduced structures $Pt/Ce_{21}O_{41}$(a-d) with Pt atoms located outside on the ceria nanoparticle. Still the square-planar coordination of the Pt atom model (e) remains the most stable for the reduced system with E_{rel} = -3.59 eV (structure e-1v in Table 1). When two O vacancies are created and Pt is inside the nanoparticle (structure f-2v), four Ce^{3+} ions are formed, i.e. here Pt acquires the oxidation state 0. The E_{rel} value for this structure, 0.87 eV, is close to that for the structures with Pt species on the surface of the nanoparticle in series a-d. Yet, the structure f-2v is less stable by ~2.5 eV than the structure e-2v.

The oxidized states of the system were studied by addition (adsorption) of one and two atoms O near the Pt atom in the stoichiometric models. The addition of one O atom (equivalent to the adsorption of a neutral PtO species on the $Ce_{21}O_{42}$ particle) results in the oxidation of Pt atom to Pt^{2+} state for the structures in series b and c. This is also confirmed by the calculated Bader charges of Pt in $PtO/Ce_{21}O_{42}$(b-c), 0.85-0.90 |e|, which are similar to the charge of Pt atom in $Pt/Ce_{21}O_{42}$(e), 0.82 |e|, where the oxidation state Pt^{2+} is unequivocally manifested by the presence of two Ce^{3+} cations. In the same way the addition of two oxygen atoms (equivalent to adsorption of PtO_2 species on the $Ce_{21}O_{42}$ particle) generates Pt^{4+} in the structures $PtO_2/Ce_{21}O_{42}$(a, c-e) as indicated by the Bader charges of Pt 1.31– 1.38 |e| (Table 1).

In some cases the oxygen addition does not result in the formation of the targeted oxidation state of platinum species, e.g. in the complex $PtO_2/Ce_{21}O_{42}$ (b) Pt is in the oxidation state +2, since peroxo (O_2^{2-}) species are formed.

The stability of the four considered Pt positions on {111} facets and edges (Fig. 1, series a-d) increases monotonously with the Pt oxidation (Fig. 2). The energy gain is the largest for Pt position (d) with $\Delta E(Pt^{2+}/Pt^0)$ = -1.98 eV and $\Delta E(Pt^{4+}/Pt^{2+})$ = -1.47 eV. For the oxidized structures $PtO/Ce_{21}O_{42}$(d) and $PtO_2/Ce_{21}O_{42}$(d) E_{rel} = -4.54 and -5.99 eV,

respectively. The structure (d) is the most stable among the studied oxidized structures with two additional oxygen atoms (corresponding to Pt^{4+} state). A small deviation from the general trend is observed in the series (b), where PtO_2 species is less stable, than PtO, by 0.51eV, probably due to formation of O_2^{2-} species.

The most stable Pt position (e) is less vulnerable towards oxidation. The energy gain due to addition of the first O atom, complex $PtO/Ce_{21}O_{42}$(e), is very small, 0.46 eV, because already in $Pt/Ce_{21}O_{42}$(e) the Pt atom in a stable square-planar complex is in the oxidation state +2. In $PtO/Ce_{21}O_{42}$(e) the Pt^{2+} oxidation state remains unchanged when one O is added, since the latter withdraws two electrons from the available Ce^{3+} centers. Addition of the second atom O is even an endothermic process. In this case two of the bridging O atoms of the square around Pt are shifted to terminal positions (bound to only one cerium center). Together with the two additional O centers (also in terminal positions) they form a new square for coordination of platinum species (see structure e-2O in Fig. 1). Platinum in this new square-planar complex is in +4 oxidation state.

3.2 Local structure of the mononuclear platinum species

In two of the considered models (a) and (d) with a neutral Pt atom, it interacts with only one O center, Pt-O distance is 194 pm. In the models (b) and (c), the Pt atom interacts with two O centers, Pt-O distances are 200 – 217 pm, while in the model (e), Pt^{2+} is bound to four O atoms with Pt-O distances of 204 – 208 pm.

$PtO_X/Ce_{21}O_{42-Y}$ systems a, b, c and d show several trends with respect to their local structures. First, creation of O vacancies does not change lengths of Pt-O bonds and their number. Second, the number of Pt-O contacts increases with the number of added O atoms. Since the oxidation state of Pt changes, addition of O atoms leads also to shrinking of Pt-O distances by ~7-10 pm. The structure b-2O deviates from this trend: there, the average Pt-O distance is longer than in the structure b-1O. As mentioned above, the reason for this deviation is formation of O_2^{2-} species with O-O distance of only 149 pm. Hence, in the structure b-2O the oxidation state of Pt remains only +2, despite that two O atoms are added. Similar to other models, creation of O vacancies in structure (e) changes neither Pt-O bond lengths nor number of contacts. Also when O atoms are added the average Pt-O distances decrease, but the number of Pt-O contacts remains unchanged.

The results of our computational studies can be compared to different types of experimental data. Important experimental structural information for the studied systems can

be obtained from Extended X-ray Absorption Fine Structure (EXAFS). EXAFS results[35] obtained under oxidation condition for Pt supported on ceria-based mixed oxide report the average Pt-O and Pt-Ce distances of 202 and 301 pm with coordination numbers 4.1 and 3.5, respectively. These values are the closest (see Table 1) to those for Pt in the position e (square-planar coordination). These are the regular structure $Pt/Ce_{21}O_{42}$-e and the structures with one or two O vacancies, which have four Pt-O and four Pt-Ce contacts with average distances of 206 and 302 pm, respectively. The structure with one additional O, $PtO/Ce_{21}O_{42}$-e, has four Pt-O and four Pt-Ce contacts with average distances of 205 and 305 pm, respectively. Two of the other structures under scrutiny also have characteristics close to the experimental ones. In the structure $PtO_2/Ce_{21}O_{42}$-c, where Pt is in oxidation state +4, the average Pt-O and Pt-Ce distances are 197 and 309 pm with coordination numbers of 4 and 3, respectively. Similarly, the average Pt-O distance, 203 pm, and coordination number, four, in one of the structures where Pt is inside the ceria nanoparticle, $Pt/Ce_{21}O_{41}$-f (oxidation state +2), are close to the experimental values, but the average Pt-Ce distance, 310 pm, and coordination number, five, are somewhat higher since in this structure the platinum species is surrounded by ceria from all sides. The latter two structures c-2O and f-1v are predicted to be less stable according to our thermodynamic model (see below). Hence, combining the computational results presented above (both the thermodynamic stability and the structural data) with EXAFS data, one can suggest that the experimentally studied Pt/CeO_2 samples likely contain Pt^{2+} species located on {100}-like facets. Moreover, it was already shown8 that this species are also the most stable on larger ceria nanoparticles.

3.3 Electronic properties of the mononuclear platinum species

Similar to the results calculated for CeO_2(111) extended surfaces,[17] the Bader charge analysis indicates that Pt atoms on $Ce_{21}O_{42}$ nanoparticle in positions (a) – (d) are almost neutral, -0.08 ÷ 0.11 |e|. The charge of Pt does not change notably, when O vacancies are created. These Bader charge values correspond to Pt in the oxidation state 0. The addition of an O atom to the system leads to oxidation of platinum species to +2 oxidation state, which is reflected in the Bader charge of Pt center, which increases to 0.62 – 0.90 |e|. The charge of the platinum center also depends on its coordination - when it is coordinated to two O centers, as in positions (a) and (d), its charge is 0.62 – 0.69 |e|. In positions (b) and (c), where the Pt atom has three O neighbors, the Bader charge of Pt is 0.85 – 0.90 |e|. In all these cases no Ce^{3+} ions are present.

When two O atoms are added, the Bader charge of Pt increases further to ~1.3 – 1.4 |e|. Only in the structure b-2O the charge is smaller 0.94 |e|, corresponding to Pt oxidation state of +2 due to already mentioned formation of peroxo species. Overall, from the Bader charge analysis one can conclude that Pt charge of -0.08 – 0.11 |e|, 0.62 – 0.69 |e|, 0.85 – 0.90 |e| and ~1.3 – 1.4 |e| correspond to Pt species in the oxidation states 0, +2 (two-coordinated), +2 (three-coordinated), and +4, respectively.

We also calculated core level energies in the initial state approximation, as a characteristic related to the oxidation state of platinum species (Table 2). Our results show that the energies of Pt 4f levels, which correspond to Pt^{2+} and Pt^{4+} species are shifted by 0.9-1.4 and 2.5-4.0 eV, respectively, from the values for the Pt^0 species (Fig. 3). The large variations in the core level shifts upon oxidation of the platinum species are likely caused by the different direction of the influence of the number of Pt-O contacts in a specific structure on the core level shifts for Pt^0, Pt^{2+} and Pt^{4+} species. The trends presented in Fig. S1 (provided in ESI) shows that Pt 4f core levels of the atomic Pt^0 are stabilized when the number of Pt-O contacts increases, while Pt 4f core levels for Pt^{4+} species are destabilized upon increase the number of the Pt-O contacts. The calculated core level shifts of the Pt^{2+} species are essentially independents on the number of Pt-O contacts. Due to these trends the positions a and d, where the platinum species has the lowest number of Pt-O contacts, show the largest core level stabilization upon oxidation from Pt^0 to Pt^{4+}, around 4.0 eV, while for position c the stabilization is only 2.5 eV.

Our estimations for the core level shifts are in qualitative agreement with experimental data, having in mind the limitations of initial state approximation approach and our reference value – Pt 4f value for atomic Pt species. Bruix et al.[8] reported the difference in the experimental core level energy for Pt^{2+} and Pt^{4+} species with respect to the value for metallic platinum of 1.5–1.7 eV and 3.0 eV, respectively. For oxidized Pt/CeO_2 catalysts Hatanaka et al.[9] reported a shift of 1.9 eV with respect to the values for reduced samples considered as containing Pt^0. Such core level shift corresponds to oxidation of platinum to +2 rather than +4 state. Several groups also reported Pt^{2+} peaks at 1.0–2.05,[36-39] or 2.4–3.0 eV[40,41] and Pt^{4+} peaks at 3.6–4.5 eV[38-40,42] relative to the peak position of Pt^0.

Interestingly, Hatanaka et al.[9] established in their XPS study of a Pt/CeO_2 catalyst that subsequent oxidation, reduction and re-oxidation of the sample results in reversible reduction and oxidation of only part of platinum species, while some of platinum remains oxidized during the treatments. Measured Pt 4f core level shift of the latter species, 1.0 eV, is within

the range of our estimates for Pt^{2+} in the square-planar position on {100} facets, 0.8 to 1.7 eV with respect to the different types of Pt^0 species. Note that according to our results, platinum species in such position is expected to remain oxidized even upon reduction of the support. Thus, our findings suggest that the species observed experimentally[9] are likely single Pt^{2+} in the square-planar position on {100} facets.

3.4 Thermodynamic modeling of the redox properties of the mononuclear platinum species depending on temperature and O_2 pressure

In order to examine, which species will prevail at certain experimental conditions, we employed a thermodynamic model outlined in Section 2. We considered three temperatures: 300, 800 and 1200 K and at these temperatures we varied the partial pressure of O_2 from 10^5 down to 10^{-6} Pa (Fig. 4 and S2).

According to the calculations, the pristine $Ce_{21}O_{42}$ nanoparticle is stable with respect to formation of vacancies at T = 300 K and $P(O_2)$ in the whole modeled range (10^{-6} - 10^5 Pa) (see Fig. S2). At 800 K our model suggests that O vacancies can be formed at $P(O_2)$ pressure below 10^{-1} Pa. Under such conditions the structure with one O vacancy starts forming and its concentration reaches a maximum at $P(O_2) = 10^{-3}$ Pa, where ~65 % of the structures have one vacancy. The structure with two O vacancies is formed at $P(O_2) < 10^{-2}$ Pa and it is dominating at $P(O_2) < 10^{-4}$ Pa. In this region $Ce_{21}O_{42}$ nanoparticle without vacancies should not exist. At T = 1200 K, all processes start at about 10^4 times higher $P(O_2)$ than at 800 K. If we want to perform the vacancy formation process at atmospheric pressure, according to our model one need to heat the sample with $Ce_{21}O_{42}$ nanoparticles to T > 1600 K, which is in agreement with the experimental results.[43] For a comparison on aggressive heating (1000 K min^{-1}) to 1773 K under an inert atmosphere ($P(O_2) = 10^{-5}$ atm ~ 1 Pa), almost immediate release of oxygen is observed experimentally,[44] which is in line with results of our thermodynamic model.

Thermodynamic model was also applied to the five series (a)-(e) of platinum-containing models $PtO_X/Ce_{21}O_{42-Y}$ (X, Y = 0 ÷ 2), considered by us (Fig. S2). At T = 300 K and $P(O_2) = 10^5$ Pa the most stable structures in the individual series are $PtO/Ce_{21}O_{42}$ or $PtO_2/Ce_{21}O_{42}$, depending on the E_{rel} value for PtO and PtO_2 for the specific series. This shows that E_{rel} value has the main contribution in our thermodynamic model in most of the cases (see Fig. 4). In the series (e), to which the most stable structures for almost all types of species belong, at the conditions T = 300 K and $P(O_2) = 10^5$ Pa PtO species prevails (with E_{rel} = -5.98 eV). At 300 K upon decrease of $P(O_2)$ below 10 Pa, this species starts to convert to

$Pt/Ce_{21}O_{42}$–e species (also containing Pt^{2+}), which are the next in stability with E_{rel} = -5.52 eV. In series (a) and (c) transition between the most stable $PtO_2/Ce_{21}O_{42}$ and the next in stability $PtO/Ce_{21}O_{42}$ species is calculated to take place at O_2 pressure below 1 Pa, while in the series (b) and (d), PtO and PtO_2, respectively, dominate in the whole range of considered $P(O_2)$ at 300 K.

When the temperature increases to 800 K, the transitions observed at 300 K are shifted to 10^5-10^6 times higher pressure (Fig. S2). In addition, new transitions take place at $P(O_2)$ below 10^{-1} Pa. For instance, for the series (e) the structures with one O vacancy start forming at $P(O_2) < 10^{-3}$ Pa, and at the lowest modeled O_2 pressures the structure with two O vacancies becomes dominant (Fig. 4, T = 800 K). At series (a) and (d) the $PtO/Ce_{21}O_{42}$ species, dominating at large region of O_2 pressure, convert directly to $Pt/Ce_{21}O_{40}$ (with two O vacancies), at $P(O_2)$ below 10^{-3} and 10^{-5} Pa, respectively. In series (b) intermediate formation of species $Pt/Ce_{21}O_{41}$ with one O vacancies is predicted at $P(O_2)$ between 10^{-2} Pa and 10^{-5} Pa. The initial $Pt/Ce_{21}O_{42}$ species dominates in large interval of O_2 pressures, 10^{-4} to 10^4 Pa, in the series (e). At lower O_2 pressure structures with one and two O vacancies are subsequently formed, while at higher pressure the $PtO/Ce_{21}O_{42}$ species appears. In series (c) with decreasing O_2 pressure the $PtO_2/Ce_{21}O_{42}$ species is subsequently converted into $PtO/Ce_{21}O_{42}$ and $Pt/Ce_{21}O_{42}$ species. The $Pt/Ce_{21}O_{42}$ species dominates in the range $10^{-3} < P(O_2) < 10^{-1}$ Pa and below 10^{-3} Pa the dominating structure is $Pt/Ce_{21}O_{40}$ with two O vacancies.

Since at 800 K at the lowest $P(O_2)$ the structures with two O vacancies are already formed in all series, no new transitions are observed when the temperature increased to 1200 K but all transitions are shifted to higher partial pressures of O_2, as expected (Fig. S2). The shift is between 2 (for higher pressures) and 5 (for lower pressures) orders of magnitude with respect to the values found for T = 800 K. Hence, both transitions become at significantly closer values of $P(O_2)$ at 1200 K compared to those at 800 K, i.e. the intermediate species ($PtO/Ce_{21}O_{42}$ or $Pt/Ce_{21}O_{42}$) in each series dominates in narrower interval of O_2 pressures.

Assuming that atomic Pt is mobile on the surface of the ceria nanoparticle, we considered also a general thermodynamic model including a series consisting of the most stable structures of each type, $PtO_X/Ce_{21}O_{42-Y}$ (X, Y = 0 ÷ 2): from position (e) for Y = 0 – 2 and X = 0 and 1, and from position (d) for X = 2. In this series the calculation results in curves, which are identical with those for position (e) (Fig. 4) since the stability of the structure $PtO_2/Ce_{21}O_{42}$–d is essentially the same as that of the structure $PtO/Ce_{21}O_{42}$ in series (e) (Table 1).

The present thermodynamic results also confirm the conclusion based on the calculated E_{vac} values that the presence of Pt on $Ce_{21}O_{42}$ hinders the O vacancy formation. In all modeled series the process starts at least at one order of magnitude lower O_2 pressure for $Pt/Ce_{21}O_{42}$ compared to pristine $Ce_{21}O_{42}$ nanoparticle (Fig. S2).

4 Conclusions

Our density functional calculations showed that the most stable sites for adsorption of mononuclear Pt species on $Ce_{21}O_{42}$ nanoparticle are at small {100} facets, in agreement with a recent study.[8] At such sites Pt forms square-planar coordination complex with four O atoms from the ceria nanoparticle. The oxidation state of Pt is +2 and two Ce^{3+} ions are formed. This oxidation state of platinum is preserved even upon reduction of the ceria support, during which more Ce^{3+} cations are created. For all other studied positions on the ceria nanoparticle (either stoichiometric or reduced) single Pt atoms remain in the oxidation state 0.

At strongly oxidation conditions, if PtO_2 species are formed, the most stable adsorption positions for them are at {111} facets. However, our thermodynamic model suggests that such species cannot be formed even at conditions close to standard (300 K; 10^5 Pa of O_2 pressure). Under such conditions PtO species is predicted to be the most stable, while if partial pressure of O_2 is decreased below 100 Pa the additional oxygen atom desorbs and the stoichiometric complex $Pt/Ce_{21}O_{42}$ is formed. Both Pt and PtO species are adsorbed at the small {100} facet and Pt^{2+} forms a square-planar complex. The geometry characteristics of these two structures agree nicely with the available EXAFS data and the estimated Pt 4f core level shift corresponds to the experimental measurements for Pt/ceria systems. The adsorbed Pt and PtO species are energetically stable with respect to sintering, while the process of agglomeration to platinum clusters is strongly exothermic for essentially neutral atomic Pt species adsorbed on {111} facets. Our theoretical study also showed that the presence of Pt^{2+} species in the most stable {100} positions slightly hinders formation of O vacancies in CeO_2 nanoparticles.

Acknowledgments. Support by Bulgarian National Science Fund (Contract DCVP 02/2), Spanish MINECO (grant CTQ2012-34969), Generalitat de Catalunya (projects 2014SGR97 and XRQTC), the FP7 program of the European Union (projects Beyond Everest and ChipCAT (Ref. Nº310191) as well as COST Action CM1104), and CPU time on BG/P at Bulgarian Supercomputing Center is gratefully acknowledged.

Electronic Supplementary Information

Figure with calculated 4f core levels of platinum species in eV versus the number of Pt-O contacts or the sum of reciprocal squares of Pt-O distances, and figure with thermodynamic models for the various modeled series $PtO_X/Ce_{21}O_{42-Y}$ (X, Y = 0 ÷ 2) and for the pure $Ce_{21}O_{42}$ at 300, 800, and at 1200 K.

References

1. H. S. Gandhi, G. W. Graham and R. W. McCabe, *J. Catal.*, 2003, **216**, 433-442.
2. J. Kašpar, P. Fornasiero and N. Hickey, *Catal. Today*, 2003, **77**, 419-449.
3. Q. Fu, H. Saltsburg and M. Flytzani-Stephanopoulos, *Science*, 2003, **301**, 935-938.
4. T. Tabakova, M. Manzoli, D. Paneva, F. Boccuzzi, V. Idakiev and I. Mitov, *Appl. Catal. B: Environ.*, 2011, **101**, 266-274.
5. O. Pozdnyakova, D. Teschner, A. Wootsch, J. Kröhnert, B. Steinhauer, H. Sauer, L. Toth, F. C. Jentoft, A. Knop-Gericke, Z. Paál and R. Schlögl, *J. Catal.*, 2006, **237**, 1-16.
6. T. Tabakova, G. Avgouropoulos, J. Papavasiliou, M. Manzoli, F. Boccuzzi, K. Tenchev, F. Vindigni and T. Ioannides, *Appl. Catal. B: Environ.*, 2011, **101**, 256-265.
7. S. D. Senanayake, K. Mudiyanselage, A. Bruix, S. Agnoli, J. Hrbek, D. Stacchiola and J. A. Rodriguez, *J. Phys. Chem. C*, 2014, **118**, 25057-25064.
8. A. Bruix, Y. Lykhach, I. Matolínová, A. Neitzel, T. Skála, N. Tsud, M. Vorokhta, V. Stetsovych, K. Ševčíková, J. Mysliveček, R. Fiala, M. Václavů, K. C. Prince, S. Bruyère, V. Potin, F. Illas, V. Matolín, J. Libuda and K. M. Neyman, *Angew. Chem. Int. Ed.*, 2014, **53**, 10525-10530.
9. M. Hatanaka, N. Takahashi, N. Takahashi, T. Tanabe, Y. Nagai, A. Suda and H. Shinjoh, *J. Catal.*, 2009, **266**, 182-190.
10. D. Pierre, W. Deng and M. Flytzani-Stephanopoulos, *Top. Catal.*, 2007, **46**, 363-373.
11. F. R. Negreiros and S. Fabris, *J. Phys. Chem. C*, 2014, **118**, 21014-21020.
12. A. Bruix, A. Migani, G. N. Vayssilov, K. M. Neyman, J. Libuda and F. Illas, *Phys. Chem. Chem. Phys.*, 2011, **13**, 11384-11392.
13. G. N. Vayssilov, Y. Lykhach, A. Migani, T. Staudt, G. P. Petrova, N. Tsud, T. Skála, A. Bruix, F. Illas, K. C. Prince, V. Matolín, K. M. Neyman and J. Libuda, *Nat. Mater.*, 2011, **10**, 310-315.
14. G. N. Vayssilov, A. Migani and K. Neyman, *J. Phys. Chem. C*, 2011, **115**, 16081-16086.
15. S. Aranifard, S. C. Ammal and A. Heyden, *J. Phys. Chem. C*, 2012, **116**, 9029-9042.
16. S. Aranifard, S. C. Ammal and A. Heyden, *J. Phys. Chem. C*, 2014, **118**, 6314-6323.
17. A. Bruix, K. M. Neyman and F. Illas, *J. Phys. Chem. C*, 2010, **114**, 14202-14207.
18. D. O. Scanlon, B. J. Morgan and G. W. Watson, *Phys. Chem. Chem. Phys.*, 2011, **13**, 4279-4284.
19. J. P. Perdew, J. A. Chevary, S. H. Vosko, K. A. Jackson, M. R. Pederson, D. J. Singh and C. Fiolhais, *Phys. Rev. B*, 1992, **46**, 6671-6687; ibid. 1993, **48**, 4978-4978.
20. G. Kresse and J. Hafner, *Phys. Rev. B*, 1993, **47**, 558-561.
21. Version VASP.4.9; http://cms.mpi.univie.ac.at/vasp/
22. G. Kresse and D. Joubert, *Phys. Rev. B*, 1999, **59**, 1758-1775.
23. V. I. Anisimov, F. Aryasetiawan and A. I. Lichtenstein, *J. Phys.: Condens. Matter*, 1997, **9**, 767-808.
24. S. L. Dudarev, G. A. Botton, S. Y. Savrasov, C. J. Humphreys and A. P. Sutton, *Phys. Rev. B*, 1998, **57**, 1505-1509.

25. C. Loschen, J. Carrasco, K. M. Neyman and F. Illas, *Phys. Rev. B*, 2007, **75**, 035115.
26. A. Migani, G. N. Vayssilov, S. T. Bromley, F. Illas and K. M. Neyman, *Chem. Commun.*, 2010, **46**, 5936-5938.
27. A. Migani, G. N. Vayssilov, S. T. Bromley, F. Illas and K. M. Neyman, *J. Mater. Chem.*, 2010, **20**, 10535-10546.
28. G. Preda, A. Migani, K. M. Neyman, S. T. Bromley, F. Illas and G. Pacchioni, *J. Phys. Chem. C*, 2011, **115**, 5817-5822.
29. D. Gryaznov, E. Blokhin, A. Sorokine, E. A. Kotomin, R. A. Evarestov, A. Bussmann-Holder, and J. Maier, *J. Phys. Chem. C,* 2013, **117**, 13776-13784.
30. S.M. Kozlov, K.M. Neyman. *Phys. Chem. Chem. Phys.,* 2014, **16,** 7823-7829.
31. J. W. Ochterski, Thermochemistry in *Gaussian*, 2000, 1-19, www.gaussian.com/g_whitepap/thermo.htm
32. N. Hansen, T. Kerber, J. Sauer, A. T. Bell and F. J. Keil, *J. Am. Chem. Soc.*, 2010, **132**, 11525-11538.
33. H. A. Aleksandrov and G. N. Vayssilov, *Catal. Today*, 2010, **152**, 78-87.
34 K. M. Neyman, C. Inntam, V. A. Nasluzov, R. Kosarev and N. Rösch, *Appl. Phys. A*, 2004, **78**, 823-828.
35. Y. Nagai, T. Hirabayashi, K. Dohmae, N. Takagi, T. Minami, H. Shinjoh and S. Matsumoto, *J. Catal.*, 2006, **242**, 103-109.
36. M.-C. Jung, H.-D. Kim, M. Han, W. Jo and D. C. Kim, *Jpn. J. Appl. Phys.*, 1999, **38**, 4872-4875.
37. J. S. Hammond and N. Winograd, *Journal of Electroanalytical Chemistry and Interfacial Electrochemistry*, 1977, **78**, 55-69.
38. S. Sharma, A. Gupta and M. S. Hegde, *Catal. Lett.*, 2010, **134**, 330-336.
39. W. Tang, Z. Hu, M. Wang, G. D. Stucky, H. Metiu and E. W. McFarland, *J. Catal.*, 2010, **273**, 125-137.
40. K. S. Kim, N. Winograd and R. E. Davis, *J. Am. Chem. Soc.*, 1971, **93**, 6296-6297.
41. C. R. Parkinson, M. Walker and C. F. McConville, *Surf. Sci.*, 2003, **545**, 19-33.
42. J. L. G. Fierro, J. M. Palacios and F. Tomas, *Surf. Interface Anal.*, 1988, **13**, 25-32.
43. W. C. Chueh, C. Falter, M. Abbott, D. Scipio, P. Furler, S. M. Haile and A. Steinfeld, *Science*, 2010, **330**, 1797-1801.
44. W. C. Chueh and S. M. Haile, *Philos. Trans. Roy. Soc. A: Mathematical, Physical and Engineering Sciences*, 2010, **368**, 3269-3294.

Tables

Table 1. Energetic, electronic, and structural characteristics of the $PtO_X/Ce_{21}O_{42-Y}$ (X, Y = 0 ÷ 2) complexes (for the structures see Fig. 1).

	E_{rel}	$BE(PtO_X)$	E_{vac}[a]	q(Pt)[b]	Ns[c]	$\#O_{vac}$[d]	$\#Ce^{3+}$[e]	#Pt-O[f]	<Pt-O>[g]	#Pt-Ce[h]	<Pt-Ce>[i]
a-2v	0.90	-2.66	3.48	-0.11	4	2	4	1	194	2	315
a-1v	-0.57	-2.25	2.01	-0.10	2	1	2	1	193	2	313
a-reg	-2.58	-2.58		-0.08	0	0	-	1	194	2	314
a-1O	-4.61	-2.74		0.62	2	0	-	2	187	2	314
a-2O	-5.26	-0.93		1.36	0	0	-	3	184	1	317
b-2v	1.27	-2.28	3.69	0.12	4	2	4	2	211	3	300
b-1v	-1.00	-2.68	1.42	0.12	2	1	2	2	211	3	301
b-reg	-2.42	-2.42		0.09	0	0	-	2	217	3	305
b-1O	-4.21	-2.33		0.85	0	0	-	3	202	2	294
b-2O	-3.70	0.63		0.94	0	0	-	4	208	3	302
c-2v	0.45	-3.10	3.50	0.09	4	2	4	2	206	2	280
c-1v	-1.05	-2.73	2.00	0.09	2	1	2	2	206	3	295
c-reg	-3.05	-3.05		0.11	0	0	-	2	206	3	296
c-1O	-4.42	-2.54		0.90	0	0	-	3	204	3	291
c-2O	-4.93	-0.60		1.31	0	0	-	4	197	3	309
d-2v	1.18	-2.37	3.75	-0.28	4	2	4	1	195	2	304
d-1v	-0.51	-2.19	2.05	-0.09	2	1	2	1	195	2	307
d-reg	-2.56	-2.56		-0.02	0	0	-	1	194	3	318
d-1O	-4.94	-3.07		0.69	2	0	-	2	186	2	319
d-2O	-5.99	-1.66		1.38	0	0	-	3	184	2	327
e-2v	-1.58	-5.13	3.94	0.81	6	2	6	4	206	4	302
e-1v	-3.59	-5.27	1.94	0.81	4	1	4	4	206	4	302
e-reg	-5.52	-5.52		0.82	2	0	2	4	206	4	302
e-1O	-5.98	-4.11		0.88	0	0	-	4	205	4	305
e-2O	-5.05	-0.72		1.34	0	0	-	4	193	0	-
f-2v	0.87	-2.68	6.40[j]	-0.05	4	2	4	2	206	4	293
f-1v	-1.47	-3.15	4.05[j]	0.81	4	1	4	4	203	5	310
exp.[k]								4.1	202	3.5	301

[a] Energy for one and two O vacancies from bare $Ce_{21}O_{42}$ nanoparticles are 1.68 and 3.55 eV
[b] Bader charge of Pt
[c] Number of unpaired electrons in the system
[d] Number of O vacancies
[e] Number of Ce^{3+} ions in the ceria nanoparticle
[f] Number Pt-O contacts
[g] Averaged Pt-O distance. Cut-off distances used in our study is 220 pm
[h] Number Pt-Ce contacts below the cut-off
[i] Averaged Pt-Ce distance. Cut-off distances used in our study is 330 pm
[j] Energy for formation of one and two O vacancies calculated with respect to the most stable regular structure, $Pt/Ce_{21}O_{42}$-e
[k] EXAFS data from Ref. 35

Table 2

Calculated core level energy shifts for Pt 4f levels in the optimized $PtO_X/Ce_{21}O_{42-Y}$ (X, Y = 0 ÷ 2) structures with respect to the value of the Pt^0 species in the $Pt/Ce_{21}O_{42}$-(a) complex. Negative values correspond to more stable core level.

X	0	0	0	1	2
Y	2	1	0	0	0
series a	0.0	-0.1	0.0	-0.9	-4.1
series b	-0.7	-0.7	-0.6	-2.0	-2.0
series c	-1.0	-0.9	-0.9	-1.9	-3.4
series d	-0.2	-0.1	-0.1	-1.7	-3.9
series e	-1.7	-1.7	-1.7	-1.8	-3.3

Figures

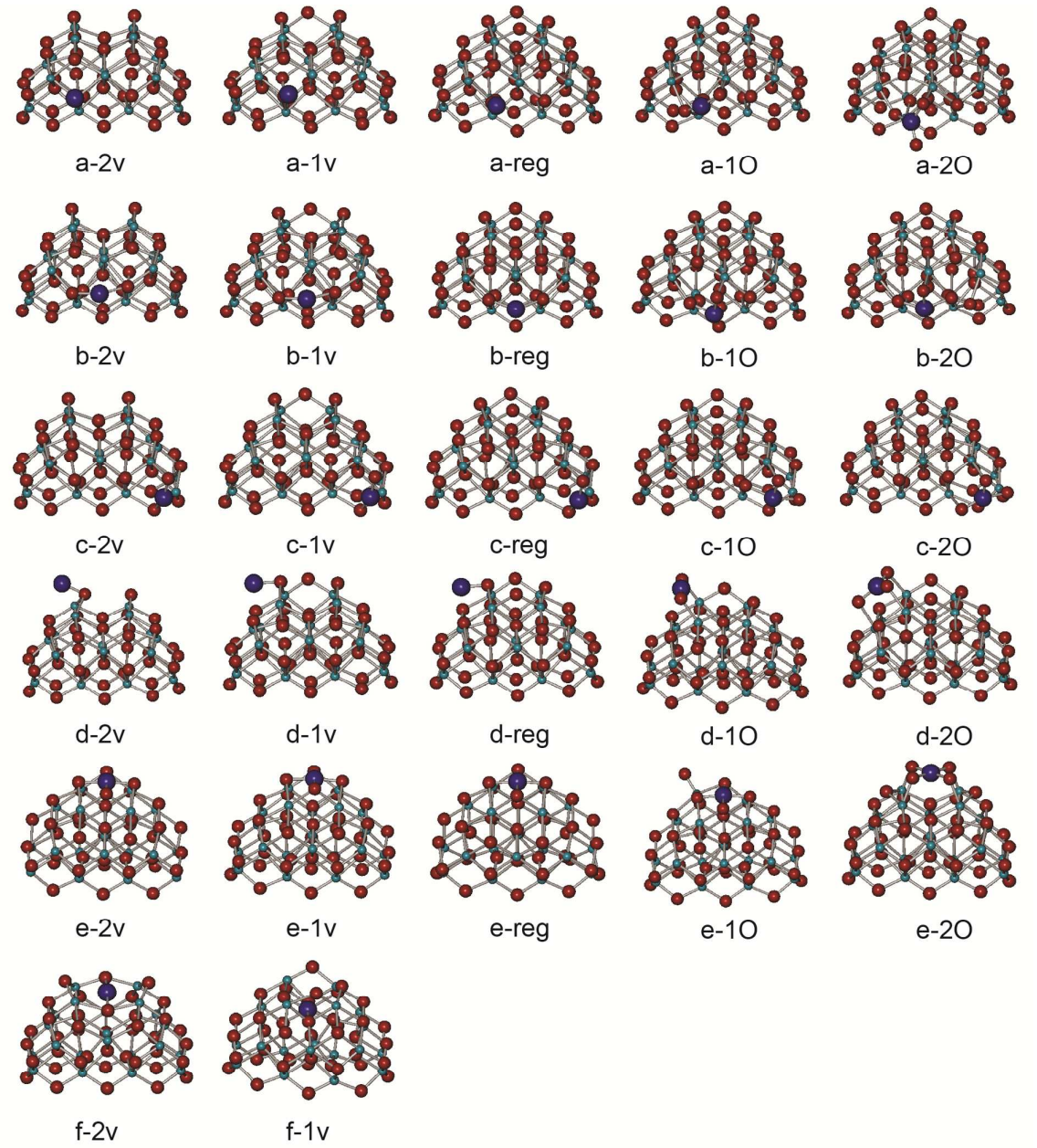

Figure 1

Optimized structures of the complexes $PtO_X/Ce_{21}O_{42-Y}$ (X, Y = 0 ÷ 2). Five different studied locations of atomic Pt on the surface of the ceria particle are labelled by letters (a) – (e). Complexes $Pt/Ce_{21}O_{42}$ in different series are labelled as reg (X = Y = 0), whereas 1O and 2O indicate addition to the reg system of one (X = 1) and two (X = 2) O atoms, and 1v and 2v denote creation in reg structure of one (Y = 1) and two (Y = 2) O vacancies, respectively. In complexes (f) platinum is located in a cavity formed from one or two O vacancies. Color coding: red – O; light blue – Ce; dark blue – Pt.

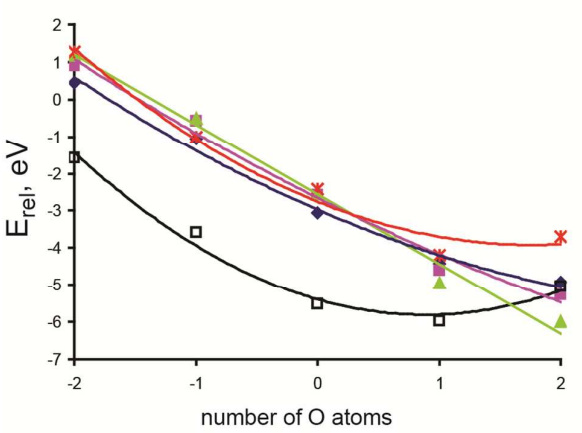

Figure 2

Dependence of relative energy, E_{rel}, of the complexes $PtO_X/Ce_{21}O_{42-Y}$ (X, Y = 0 ÷ 2) in different series on the number of removed or added O atoms. E_{rel} is calculated with respect to the bare stoichiometric ceria nanoparticle, Pt atom and corresponding amount of O_2 molecules in the gas phase. Series a (violet - ■), series b (red -∗), series c (dark blue - ♦), series d (green - ▲), series e (black - □).

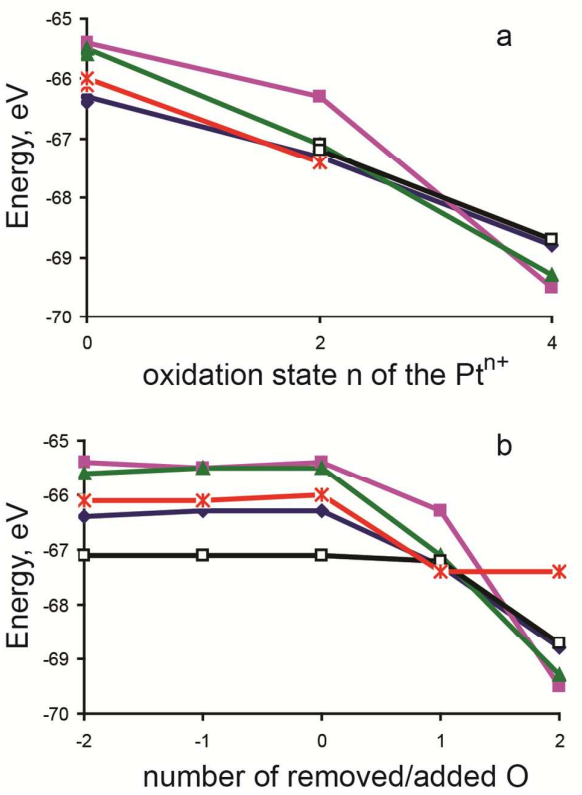

Figure 3

Relative energies of Pt 4f levels (a) versus assumed oxidation state n of the Pt^{n+} species (see discussion in the text) and (b) versus number of removed/added O to the system in different locations on ceria nanoparticle: series a (violet - ■), series b (red -✳), series c (dark blue - ♦), series d (green - ▲), series e (black - □).

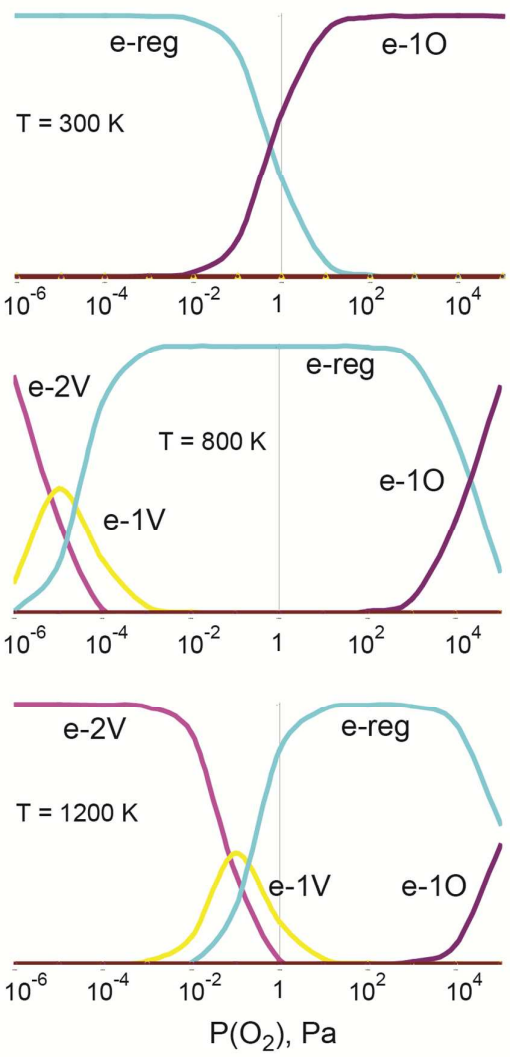

Figure 4

A general thermodynamic model including a series consisting of the most stable structures of each type, $PtO_X/Ce_{21}O_{42-Y}$ (X, Y = 0 ÷ 2): from position e for Y = 0 – 2 and X = 0 and 1, and from position d for X = 2 at three different temperatures. The vertical axis corresponds to the relative concentration of the species ranging from 0 to 100%.